Lethal interactions of atomically precise gold nanoclusters and *Pseudomonas aeruginosa* and *Staphylococcus aureus* bacterial cells

Denver P. Linklater,[a] *Xavier Le Guével,*[b] *Gary Bryant,*[a] *Vladimir A. Baulin,*[c] *Eva Pereiro,*[d] *Palalle G.Tharushi Perera,*[a] *Jason V. Wandiyanto,*[e] *Saulius Juodkazis,*[e] *Elena P. Ivanova*[*a]

[a] STEM College, School of Science, RMIT University, Melbourne, Victoria, 3001, Australia

[b]Cancer Targets and Experimental Therapeutics, Institute for Advanced Biosciences, University of Grenoble Alpes, Site Santé - Allée des Alpes, La Tronche, 38700, France

[c] Departament de Química Física i Inorgànica, Universitat Rovira i Virgili, C/ Marcel.lí Domingo s/n, Tarragona, 43007, Spain

[d] MISTRAL Beamline-Experiments Division, ALBA Synchrotron Light Source, Cerdanyola del Vallès, Barcelona, 08290, Spain

[e] Optical Sciences Centre, Swinburne University of Technology, Hawthorn, Victoria, 3122, Australia

KEYWORDS: ultrasmall metal nanoclusters, gold nanoclusters, antimicrobial effect, cytotoxicity, translocation

ABSTRACT

Ultrasmall metal nanoclusters (NCs) are employed in an array of diagnostic and therapeutic applications due to their tunable photoluminescence, high biocompatibility, polyvalent effect, ease of modification and photothermal stability. However, AuNCs' intrinsically antimicrobial properties remain poorly explored and are not well-understood. Here, we share an insight as to the antimicrobial action of atomically precise gold nanoclusters (AuNC) based on their ability to passively translocate across the bacterial membrane. Functionalised by a hydrophilic modified-bidentate sulfobetaine zwitterionic molecule (AuNC-ZwBuEt) or a more hydrophobic monodentate-thiolate (AuNC-MHA) molecule, 2 nm AuNCs were lethal to both Gram-negative *Pseudomonas aeruginosa* and Gram-positive *Staphylococcus aureus* bacteria. The bactericidal efficiency was found to be bacterial strain-, time-, and concentration-dependent. The direct visualisation of the translocation of AuNCs and AuNC-cell and subcellular interactions were investigated using cryo-soft X-ray nano-tomography (Cryo-SXT), transmission electron microscopy (TEM), and scanning TEM-energy dispersive spectroscopy (STEM-EDS) analyses. AuNC-MHA were identified in the bacterial cytoplasm within 30 min, without evidence of the loss of membrane integrity. It is proposed that the bactericidal effect of AuNCs is attributed to their size, which allows for efficient energy-independent translocation across the cell membrane. The internalisation of both AuNC caused massive internal damage to the cells, including collapsed subcellular structures, altered cell morphology, leading to the eventual loss of cellular integrity.

1. INTRODUCTION

Gold nanoclusters (AuNC), consisting of an assembly of a defined number of atoms (typically between tens and hundreds), exhibit distinct electronic states enabling tunable photoluminescence from the ultraviolet (UV) to the near infrared (NIR) wavelength regions.[1] Owing to their photoluminescence properties in the near infrared/shortwave infrared (NIR/SWIR) region, AuNCs can be tracked in real-time in various organs, making them an important diagnostic and therapeutic tool.[2-3] For example, it has recently been demonstrated that ultra-small AuNC (core diameter <2 nm), protected by thiolate ligands, facilitate excellent *in vivo* computed tomography (CT) imaging, particularly of tumours.[4-7]

AuNCs have also recently been found to act as potent antimicrobial agents toward both Gram-negative[8-9] and Gram-positive bacteria.[10] For therapeutic applications, AuNCs conjugated with various surface ligands have been extensively researched as antimicrobial agents owing to their high biocompatibility, polyvalent effect, ease of modification and photothermal stability.[11-12] Many research groups have focused on employing AuNCs conjugated to antibiotics, amino acids, antibacterial peptides, and quaternary ammonium compounds, to demonstrate their antibacterial efficacy.[13-16] The antibacterial action of antimicrobial conjugated AuNCs has been attributed to their ultra-small size and high surface area allowing for increased opportunity for interaction with bacteria in suspension and efficient binding of antibacterial small molecules at the bacterial membrane.[16-17] Nevertheless, AuNCs are also intrinsically antimicrobial.[10] Positively charged AuNC may promote antibacterial efficacy due to electrostatic adsorption at the negatively charged cell wall, leading to the disruption of membrane integrity, increased membrane permeability, and dissipation of membrane potential.[11, 18-19] Nevertheless, recent investigations of the antibacterial action of AuNC protected by ligands with increasingly *negative* surface charge showed that the more negatively charged AuNCs possessed greater lethal action.[17] Zheng *et al.*, recently ascribed the bactericidal properties of 0.1 mM ~2 nm AuNC to their cellular internalisation leading to the inducement of a metabolic imbalance in cells, reactive oxygen species (ROS) production, and consequent bacterial death; however, AuNC translocation was not explicitly shown.[10, 20] In another recent work, glutathione-conjugated AuNCs were shown by *in-situ* liquid cell TEM experiments to aggregate at the bacterial membrane and then penetrate the cell causing an increase in intracellular ROS and destroying the membrane integrity[21]. Contrastingly, other studies on the bactericidal action of ultra-small (3 nm) AuNPs showed no production of intracellular ROS.[22-23] Similarly, investigations of the photosensitizing capabilities of AuNC in bacteria showed that the ultra-small particles are highly capable of quenching any ROS produced.[24] Notably, while ROS generation is a reliable indication of the metabolic imbalance of cells (endogenous redox imbalances can be caused by damage, that lead to an inability of the cell to maintain redox homeostasis),[25] these indirect methods to study the antimicrobial action of AuNC have been unable to resolve single particles and their fate within the cell. Thus, the limited understanding of the antibacterial action opens the door to further investigations toward elucidating the antibacterial nature of AuNC.

At the cellular level, AuNC size, surface chemistry, and hydrophobicity are identified to influence particle interactions with biological components and cell particle uptake.[26-29] Indeed, the high diffusivity of AuNC across biological barriers at the tissue and cellular levels has been reported.[4, 30-31] Dissipative particle dynamics were previously used to shed light on the two main translocation pathways of nanoparticles of different shape by active and passive physical penetration into a cell.[32] Computer simulations concluded that the shape effect of nanoparticles was negligible at very small nanoparticle size (radius $r = 0.8$ nm) but as the particle increased in volume and radius ($r = 3.2$ nm), effects on penetration became more obvious. A similar conclusion was made from the simulation of equilibrium insertion of 2.3 nm objects into a lipid bilayer.[33] The effect of shape was found to be negligible for small radii particles and their cell-surface interactions are largely governed by surface properties. The small size (< 2 nm) of AuNCs provide them with very high surface area *versus* volume ratio and high diffusivity that allows them to translocate passively inside the cell by Brownian motion.[34] However, further clarification is required as to the effect of the AuNC functionality on their targeting, biodistribution, and toxicity toward bacteria. While the bactericidal effect of positively charged, pyrimidine-capped 3 nm AuNP was reported due to multiple sub-cellular interactions,[8] to the best of our knowledge the nature of the bactericidal efficacy of AuNC of variable degree of hydrophobicity and/or lipophilicity remains unclear. Thus, in the current work, we investigated the antibacterial mode of action of 2 nm AuNC modified with either a moderately hydrophobic monodentate-thiolated molecule or a more hydrophilic modified-bidentate sulfobetaine zwitterionic molecule to control cell-membrane interactions. The fate of AuNC in both bacterial species *Staphylococcus aureus* CIP 65.8^T and *Pseudomonas aeruginosa* ATCC 9721 was elucidated using a combination of advanced electron microscopy such as TEM, STEM-EDS, and cryo-soft X-ray tomography (Cryo-SXT).

2. RESULTS

2.1. Synthesis and characterization of AuNC

AuNC generally possess a metal core size between 1 nm and 3 nm with the Au core protected by ligand shells (Figure 1). In this study, Au_{25}NC were synthesized with a hydrophilic monodentate-thiolated molecule, mercaptohexanoic acid (MHA) containing a short aliphatic chain with a terminal carboxyl group which decorated the particle surface with negatively charged surface groups (ζ=-21.3 ± 0.5 mV), without significantly increasing particle size due to the very thin organic shell.[35-37] Another thiolated ligand, ZwBuEt, was used to produce AuNCs with lower surface hydrophobicity than AuNC-MHA while keeping a negative charge surface (ζ=-10.0 ± 0.2mV) and good colloidal stability in water and in biological media, as we reported previously.[27] Additionally, reported logP values for the surface ligands (MHA: 1.43; ZwBuEt: -3.45) confirm a large difference in the lipophilicity of the capping molecules (the more positive value corresponding to greater lipophilicity). Further characteristics of the AuNC are provided in Table S1.

Small Angle X-ray Scattering (SAXS) was used to approximate the size and shape of the particles, assuming a square prism model (*i.e.*, a faceted rod) (Figure 1C). The AuNC were determined to be square prisms with lengths of ~2.3 nm and a width of ~0.75 nm, with slight differences between the samples. Both AuNC-MHA and AuNC-ZwBuEt were found to have a faceted rod-shape geometry. A similar rod-like structure has been also reported for Au_{25} and Au_{37} gold nanoclusters that were stabilized by using small thiolated molecules.[38-40] The SAXS measurements confirmed the AuNC suspensions remained stable in suspension over the course of the 4 h measurement. AuNCs coated with zwitterionic molecules have been shown to be stable in water, buffer solution and physiological medium for approximately 6 months.[27, 41]

The AuNCs showed the characteristic UV-VIS absorption patterns of ultra-small Au particles with strong UV absorption (Figure 1D). AuNC-MHA exhibited a shoulder peak at 440 nm and a near infrared band centred at 670 nm commonly attributed to a 25-Au atom crystal structure.[37]

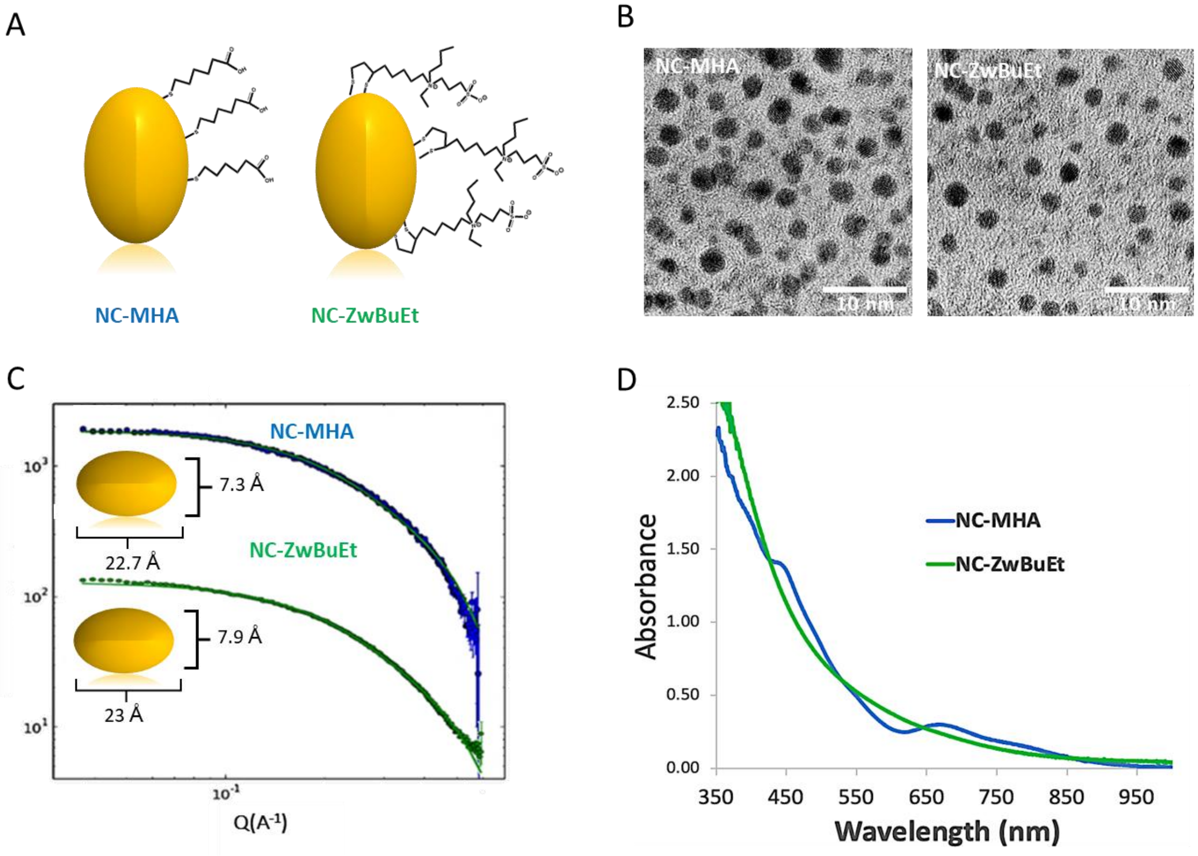

Figure 1. Synthesis and Characterisation of AuNCs. (A) Cartoon of AuNC-MHA and AuNC-ZwBuEt. (B) HRTEM images of AuNC-MHA and AuNC-ZwBuEt. (C) Fit of SAXS scattering curve, to square prism model, achieving shape parameters for AuNC-MHA of a square prism with 0.73 nm sides and a length of 2.27 nm and for AuNC-ZwBuEt a square prism with sides of 0.79 nm and length of 2.32 nm. (D) UV-VIS absorbance spectra of AuNC in water.

2.2. Ligand-surface hydrophobicity dependent antibacterial activity of AuNC

The antibacterial efficacy of AuNC-MHA and AuNC-ZwBuEt toward infectious doses of Gram-positive *S. aureus* and Gram-negative *P. aeruginosa* bacteria was evaluated for a maximum incubation period of 2h at concentrations of 5-200 µg Au mL^{-1}, as it was previously reported that 2 h incubation time was sufficient for assessment of the antimicrobial action of AuNCs.[10, 17, 20] Viable cells were quantified by colony forming units (CFU) obtained *via* the plate counting technique (Figure 2).

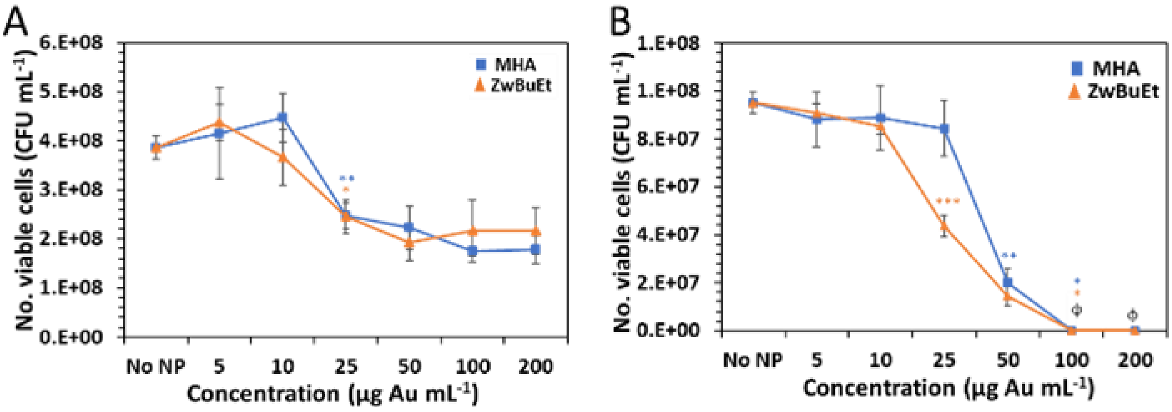

Figure 2. Antibacterial activity of AuNC as a function of concentration toward (A) *S. aureus* and (B) *P. aeruginosa* as determined by CFU mL^{-1}. Bacteria were exposed to AuNC for 2 h. Statistical significance is denoted by ***$p < 0.001$, **$p < 0.01$ and *$p < 0.05$. ϕ indicates measurement was below detection limit (minimum bactericidal concentration; MBC). Error bars are one standard deviation.

The AuNCs exhibited negligible antibacterial effect at concentrations <25 µg Au mL^{-1}. At 25 µg Au mL^{-1}, a significant drop in CFU mL^{-1} was recorded for both AuNCs (AuNC-MHA $p = 0.01$; AuNC-ZwBuEt p = 0.03) toward *S. aureus* (approximately 30% reduction in viable cells). A further 6% and 15% reduction in viable bacteria was recorded at 50 µg Au mL^{-1} AuNC-MHA and AuNC-ZwBuEt, respectively. At larger concentrations (100 and 200 µg Au mL^{-1}), the antibacterial efficacy of both AuNCs toward *S. aureus* plateaued. Interestingly, no significant difference in antimicrobial efficacy toward *S. aureus* was observed between AuNC-MHA and AuNC-ZwBuEt. By contrast, AuNC-MHA and AuNC-ZwBuEt completely inhibited the proliferation of *P. aeruginosa* with a minimum bactericidal concentration (MBC) of 100 µg mL^{-1} (Figure 2B). While ≤25 µg Au mL^{-1} AuNC-MHA had little to no effect on the growth and proliferation of *P. aeruginosa*, 25 µg Au mL^{-1} of AuNC-ZwBuEt reduced the number of viable by approximately 45% ($p = 0.0002$). These results are in good agreement with the reduction in cell viability observed at higher bacterial densities (Figure S1).

Dynamic antibacterial studies showed that as the dose of AuNC increased, the antibacterial efficiency towards both *S. aureus* and *P. aeruginosa* increased over continued contact with bacterial cells in suspension (Figure S2), demonstrating both time- and dose-dependent antibacterial activity. At 200 µg Au mL^{-1}, AuNC MHA and AuNC ZwBuEt inactivated 86% and 100% of *P. aeruginosa* bacterial cells in suspension in 30 min, respectively. Generally, the results of the plate counting technique indicated that AuNC-MHA displayed greater bactericidal activity towards *S. aureus* and *P. aeruginosa* at all incubation times tested than its less hydrophobic counterpart, AuNC-ZwBuEt.

2.3. Investigation of the interaction between AuNCs and subcellular structures

A combination of complementary electron microscopy techniques was used to directly visualize cell membrane, cell morphology, cellular integrity and AuNC interactions with subcellular structures at 2 h following incubation with 100 µg Au mL^{-1} (MBC) (Figure 3). Cross-sectional TEM analysis of bacteria incubated with ultra-small AuNC revealed significant morphological changes to the cytosol and a lack of homogeneity most likely due to the damage of intracellular structures of both *S. aureus* and *P. aeruginosa* bacterial cells. Both aggregates and single AuNC were observed within the bacterial cells at 2 h of incubation. TEM images showed the presence of single AuNC or aggregates of AuNC with cytoplasmic material corresponding to the areas with black contrast (Figure 3A). Particle analysis of clusters of AuNC-ZwBuEt and AuNC-MHA associated with *S. aureus* and *P. aeruginosa* returned a wide size distribution of

AuNC, between 5 – 30 nm. The diameters of particles that are external (E) and internal (I) to the cells are shown in Figure 3C. Aggregates of AuNC-ZwBuEt of minimum diameter 8.5 nm and maximum diameter 25 nm (corresponding to 10-12 AuNC) were observed to be embedded in the peptidoglycan layer and membrane of both *S. aureus* and *P. aeruginosa*, whereas internalised AuNC-ZwBuEt aggregates were estimated to have a mean diameter of 8 ± 2 nm. By contrast, AuNC-MHA localised in cytosolic-particle aggregates inside the bacterial cells, as seen in Figure 3Aii and 3Avi, possessed a mean diameter of 5 ± 2 nm. The diameter of AuNC-MHA particle aggregates attached externally to the cell wall of *S. aureus* ranged widely from 8.2 – 33 nm (average diameter 19.1 ± 7.5 nm). No AuNC-MHA aggregates were observed external to *P. aeruginosa* cells. Detailed TEM analysis revealed that many *P. aeruginosa* and *S. aureus* cells possessed intact double membranes (Figure S3), indicating that AuNC-MHA may be translocating across the membrane. Indeed, analysis of both TEM and SEM micrographs showed that no AuNC-MHA aggregates were observed bound externally to the cell wall (Figure 3A, 3B). SEM analysis of *P. aeruginosa* morphology showed the collapse of the central region of the cell, without the obvious leakage of cytoplasmic material.

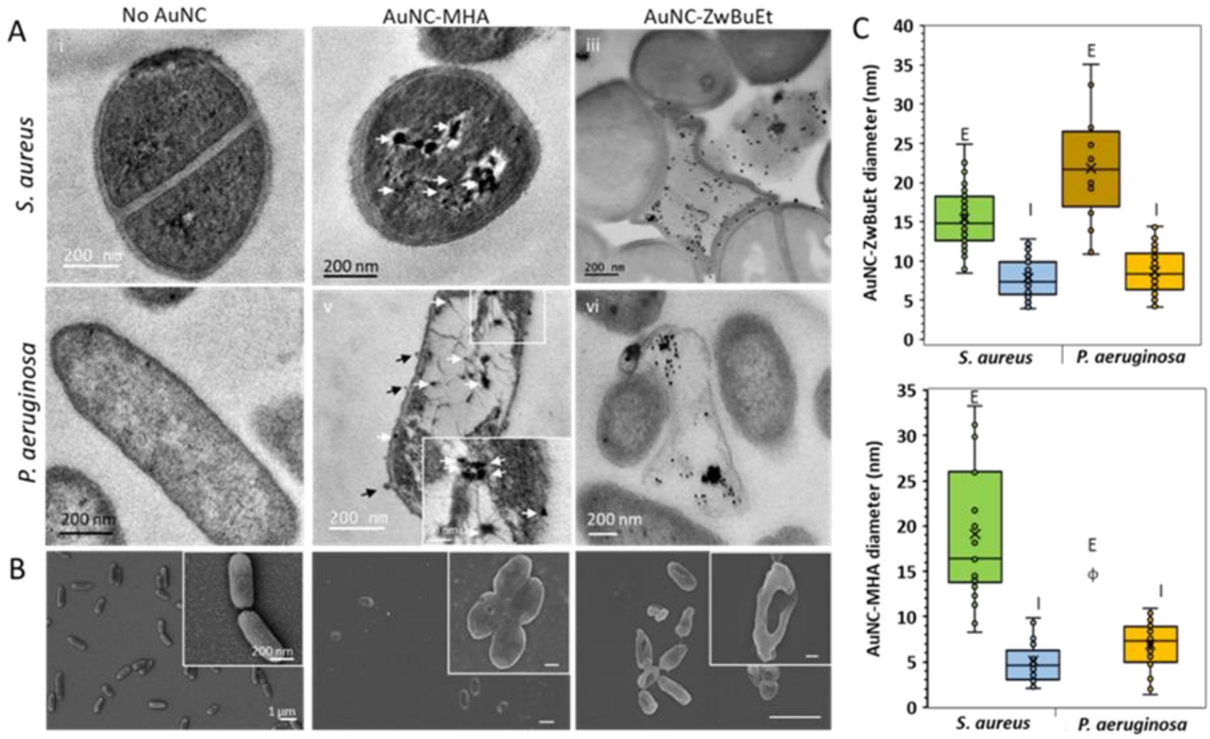

Figure 3. (A) TEM micrographs of *S. aureus* and *P. aeruginosa* incubated with no AuNC (control), and 100 µg Au mL^{-1} AuNC-MHA, and AuNC-ZwBuEt, respectively, for 2 h. Black arrows point to the bacterial structural damage incurred during incubation; white arrows indicate intracellular AuNC. AuNC-MHA localised in cytosolic-particle aggregates inside the bacterial cells, as seen in Figure 3Aii and 3Avi. Inset micrographs show AuNC-cytoplasm aggregates (white arrows) and membrane blebbing (black arrows) in response to bacterial interaction with AuNC-MHA. (B) SEM micrographs of *P. aeruginosa* morphology following 2 h incubation with no AuNC (control), and 100 µg Au mL^{-1}AuNC-ZwBuEt and AuNC-MHA, respectively. No AuNC are observed to be bound externally to *P. aeruginosa* cells; however, AuNC were observed bound to lysed cell cytoplasmic material, as observed in Figure S4. (C) Distribution of the diameter of AuNC-ZwBUEt particles observed external, E, to the cell (embedded in the peptidoglycan or membrane layers) and localised internally, I. ϕ refers to below detection limit. Statistics were performed on data analysed from an average of 50 cells per condition.

2.4. Observation of the translocation of AuNC

In-depth TEM analysis showed that the AuNC-MHA-cell interactions that led to non-viability in gram positive and gram-negative bacteria may stem from particles binding internally, and not at the cell membrane, since many cells show the destruction of internal cell integrity while simultaneously possessing intact double membranes (Figure S3). Additionally, fluorescence microscopy was used to confirm the uptake of AuNC-ZwBuEt in *P. aeruginosa* cells by exploiting the intrinsic fluorescence of the AuNCs in the NIR region (Figure S5; Figure S6). Both AuNC-MHA, and AuNC-ZwBuEt may be efficiently up-taken by bacteria, although their cell-membrane interactions appear to be highly surface-ligand dependent. Therefore, we used cryo-soft-X-ray nano-tomography to determine the initial interactions of AuNCs with *P. aeruginosa* cells at a shortened incubation time of 15 min. Cryo-SXT is advantageous over electron microscopy techniques because the cell can be imaged without the introduction of artefacts caused by fixation and staining procedures, as well as sectioning. *P. aeruginosa* cells interacting with 100 µg Au ml-1 AuNC-ZwBuEt for 15 min showed the presence of small internal inclusions[22-23] (indicated by the green arrows in Figure 4). The presence of small internal inclusions was previously reported [22-23]; however, it was not possible to identify AuNC surrounding, or internal to, these inclusion bodies. The bacterial membrane was roughened, possibly from loss of turgor pressure, in comparison to the smooth cell membrane appearance of control cells (Figure S7). Similarly, *P. aeruginosa* bacteria incubated with AuNC-MHA exhibit a damaged morphology with wrinkling of the cell wall. In the case of single particles, or small aggregates (< 20 nm), the Cryo-SXT technique may not resolve their presence inside the cell, because the spatial resolution is limited to 26 nm half-pitch.[42] After 1 h incubation, *P. aeruginosa* cells treated with AuNC-ZwBuEt showed the increased vacuole-like spaces. In the high magnification image, many of the inclusion bodies have travelled to the outer perimeter of the cell, possibly in an attempt to efflux the AuNC from the cell. *P. aeruginosa* cells treated with AuNC-MHA for 1 h appeared ruptured, in agreement with the above TEM images.

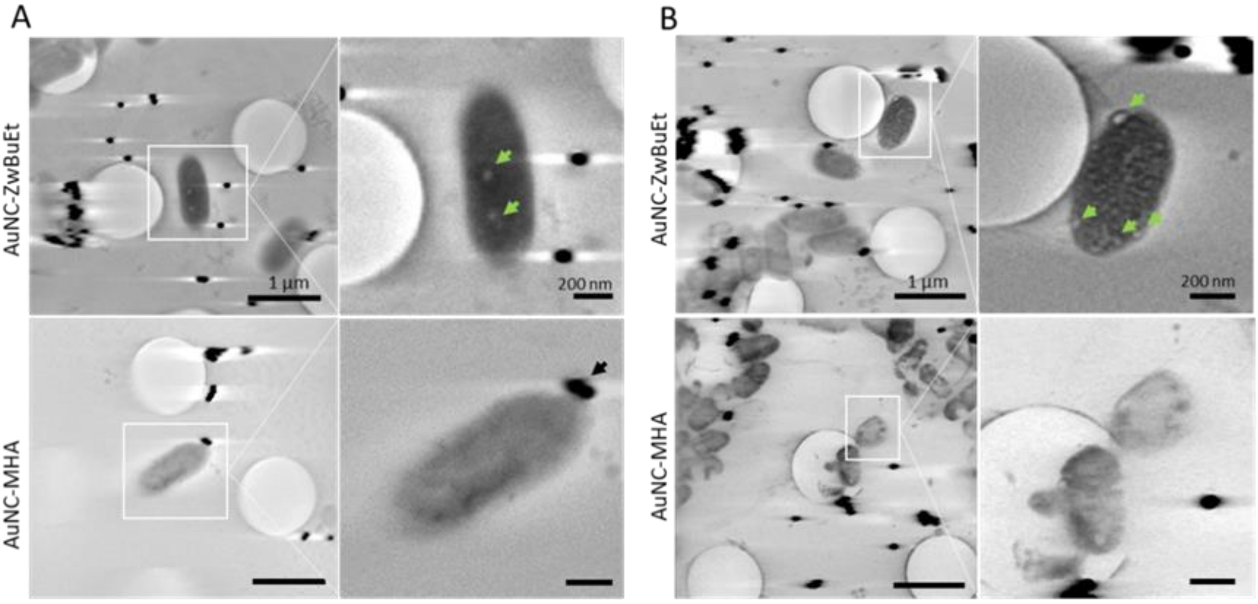

Figure 4. Aligned and reconstructed Cryo-SXT tomograms of *P. aeruginosa* morphology following (A) 15 min and (B) 60 min of interaction between bacteria and 100 µg Au mL^{-1} AuNCs. Green arrows indicate the presence of bacterial inclusions in bacteria incubated with AuNC-ZwBuEt. The black arrow indicates a 100 nm gold fiducial used for tomogram alignment.

STEM-EDS analysis as another independent complementary technique, was used to study the AuNC interaction with bacteria over 30, 60 and 120 min and to confirm the internalisation of AuNC-MHA and AuNC-ZwBuEt at each investigated time point (Figure 5). EDS analysis detected AuNC-MHA internalised in *P. aeruginosa* by 30 min whereas they were only localised inside *S. aureus* bacteria after 60 min incubation (Figure 5C; Figure 5D). Many AuNC-MHA aggregates observed in contact with *S. aureus* were found embedded in the outer peptidoglycan layer (Figure 5D), as previously determined *via* TEM (Figure 3A). For *P. aeruginosa*, at 30 min, no obvious cellular damage occurred despite EDS confirmation of the dispersal of AuNC-MHA throughout the cell cytoplasm (Figure 5C); however, at 60 min, the bacteria exhibit loss of cytosolic contents and cellular integrity (Figure 5A). Thus, we propose that intracellular accumulation of AuNC-MHA over the first 60 min of incubation led to internal damage by AuNC interaction with subcellular structures.

AuNC-ZwBuEt aggregates were only visible attached to the outer peptidoglycan layers of *S. aureus* cells at 30 min incubation (Figure 5B). However, at 60 min, AuNC-ZwBuEt were localised within the cytoplasm and obvious internal degradation had occurred (Figure 5D). Conversely, AuNC-ZwBuEt were only detectable within *P. aeruginosa* cells at 120 min of incubation.

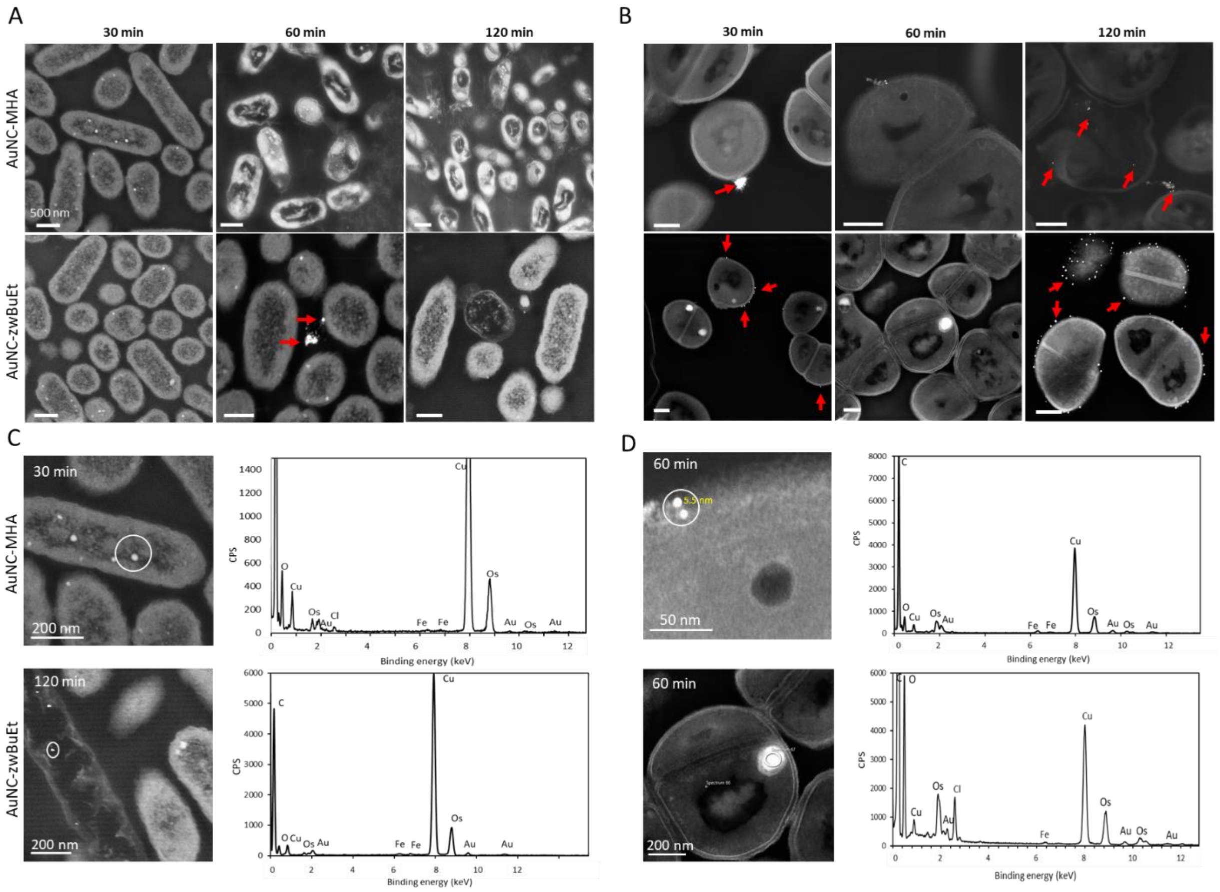

Figure 5. STEM analysis of bacteria-AuNC interactions at 30-, 60-, and 120-min. (A) STEM-EDS confirmation of the presence of Au in *S. aureus* (top panel) and *P. aeruginosa* (bottom panel) after incubation with 100 µg Au mL^{-1} AuNC-MHA and AuNC-ZwBuEt for 60 min. Bacteria were exposed to 100 µg Au mL^{-1}. Red arrows indicate observable aggregates of AuNC. (B) STEM micrographs and corresponding EDS spectra obtained from the areas within the white circles to confirm the presence of Au for (C) *P. aeruginosa* and (D) *S. aureus*. EDS spectra obtained at different incubation points are shown in Figures S8-S11.

Additionally, *in vitro* tests to assess whether the condensation of chromatin might occur because of AuNC presence inside *P. aeruginosa* cells were conducted using the high resolution Airyscan capability of a Zeiss confocal laser-scanning microscope. In agreement with TEM images, no changes to DNA localisation were detected at 30 min exposure to either AuNC. However, following 60 min exposure, some bacteria show the condensation of DNA material, clearly observed in Figure 6. Furthermore, DNA damage was assessed using a DNA ladder assay. No DNA fragmentation was visible *via* gel electrophoresis and a higher proportion of DNA breaks were not observed (Figure S12; Table S2). To further confirm that AuNC-MHA and AuNC-ZwBuEt are not preferentially targeting bacterial DNA, bacteria were treated with AuNC functionalised with arginine (AuNC-Arg) (100 μg Au mL^{-1} for 1 h), stained with DAPI, and imaged under a fluorescence microscope (Figure S13). Arg-coated AuNPs are known to interact with, and bind to, DNA.[43] Fluorescence micrographs reveal evidence of DNA damage *via* the filamentous appearance of *P. aeruginosa* cells because of an inability to correctly replicate.[44] By contrast, no such replicative errors were observed during exposure of *P. aeruginosa* and *S. aureus* to AuNC-MHA and AuNC-ZwBuEt. Further examination of TEM images of *P. aeruginosa* incubated with AuNC-MHA revealed that the bacterial DNA, although condensed inside the cell, is not directly targeted by the AuNC, as evidenced by the retention of the bacterial nucleoid and appearance of cytosolic-AuNC aggregates in a separate area of the cell (Figure 6B). Thus, the antimicrobial action of AuNC is not likely to be linked to the direct binding with nucleic acids. Alternatively, we suggest that the AuNC may form protein complexes with the cytoskeletal network, causing the condensation of chromatin as observed in Figure 6.[45]

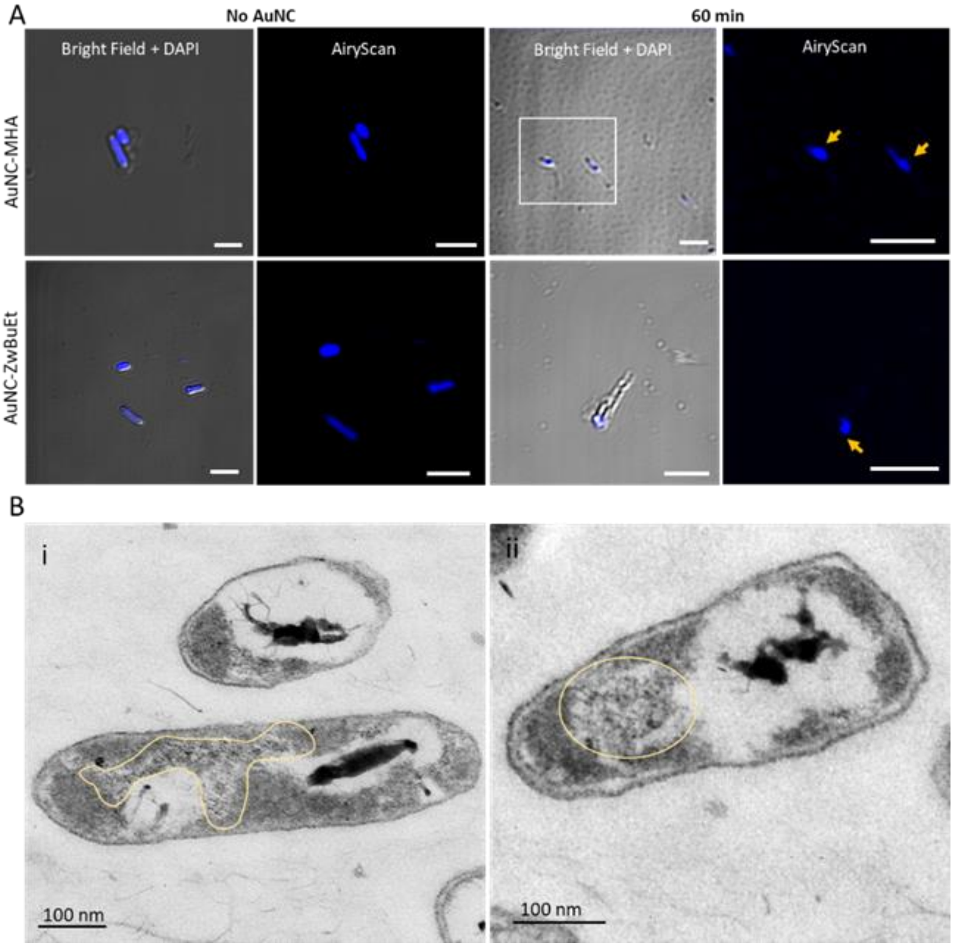

Figure 6. (A) CLSM micrographs of *P. aeruginosa* incubated with 100 µg Au mL^{-1} AuNC-MHA and AuNC-ZwBuEt for 1 h. Yellow arrows indicate DNA or chromatin condensation within the cell. Scale bars are 5 µm. (B) TEM micrographs of *P. aeruginosa* incubated with 100 µg Au mL^{-1} AuNC-MHA for 1 h. Yellow outlines highlight the condensed nucleoid of the bacterial cell.

3. DISCUSSION

It has been commonly believed that more positively charged NPs will favour interaction with the negatively charged bacterial cell wall,[46] leading to greater bactericidal efficacy; however, recent studies of thiolate-protected AuNC have shown that more negatively charged AuNCs possess greater antimicrobial efficacy.[17] In this work, there was no apparent difference between the overall antimicrobial efficacy toward *S. aureus* and *P. aeruginosa* bacteria of either AuNC studied at 2 h; however, AuNC-MHA were able to kill both bacteria more quickly, possibly explained by an increased affinity of AuNC-MHA (less negatively charged) for interaction with the hydrophobic, negatively charged bacterial cell wall.[47] Indeed, the bactericidal efficiency of the AuNC was correlated to the direct translocation of the AuNC into the cytoplasm. STEM-EDS analysis corroborated that the more potent antibacterial action of AuNC-MHA particles could be due to the efficiency with which they can enter the cell and bind to internal cell substructures. For example, where AuNC-ZwBuEt particles were observed to aggregate at the cell wall, or become embedded in the membrane, hydrophilic (and more lipophilic) monodisperse AuNC-MHA was localised within the cell interior within 30 min (in *P. aeruginosa*). Indeed, AuNC-ZwBuEt showed negligible antibacterial activity towards *P. aeruginosa* within the first 30 min of incubation at concentrations lower than 200 μg Au mL^{-1}.

Additionally, the variation of antibacterial efficacy of AuNC-MHA and AuNC-ZwBuEt was shown to be strain-species-dependent. Our work demonstrates that Gram-negative *P. aeruginosa* bacteria were generally more susceptible to the antibacterial action of both AuNC functionalised with either the monodentate-thiolate (AuNC-MHA) molecule or the modified-bidentate sulfobetaine zwitterionic molecule (AuNC-ZwBuEt) than Gram-positive *S. aureus*. The differences in cell-NP interactions between AuNC-MHA and AuNC-ZwBuEt and bacteria may be attributed to their respective surface functionalisation (surface hydrophobicity/lipophilicity and surface charge). For example, changes to AuNC surface hydrophobicity may be correlated to greater or less efficient translocation across the peptidoglycan and membrane layers of the bacterial cells.[10, 17, 48] AuNPs protected by solution facing carboxylic acid groups, such as 6-MHA, are highly stable in water and are not easily driven to aggregate by hydrogen bonding.[49] Additionally, when comparing surface ligand properties (Table S1), MHA possess a logP value of 1.43, in comparison to -3.45 for ZwBuEt, highlighting the increased lipophilicity of the compound. In turn, *S. aureus* possess a thick peptidoglycan layer that may inhibit the efficient translocation of small particles, or cause AuNC to aggregate at the cell wall, becoming embedded. Previous reports of the antibacterial action of silver ions have demonstrated that, for gram-negative bacteria, the inadequate thickness of the cell wall (composed of a thin 8 nm inner peptidoglycan layer and a 1-3 nm outer layer of liposaccharides) increases their susceptibility to the uptake of silver ions. By contrast, gram-positive bacteria are resistant to the antimicrobial action of silver ions due to the increased thickness of their cell wall (consisting of a thick 80 nm peptidoglycan layer composed of teicoic acids).[46]

The relationship between AuNC-cell membrane interaction and surface charge is less clear. Simple electrostatic arguments propose that oppositely charged NPs and membranes favour the formation of NP-lipid complexes, often leading to transient membrane damage or lipid extraction.[50-51] However, NP toxicity can occur even when the membrane and the NP have the same charge.[52-53] Furthermore, regardless of charge, both cationic and anionic AuNPs with a core diameter between 2-8 nm have been shown to passively interact with lipid membranes.[54-55] Recently, it was shown that the integrity of neutral (zwitterionic) lipid membranes was not altered by cationic or anionic thiol-protected AuNPs of 3-4 nm core diameter,[56] suggesting that factors other than charge (like NP shape and size) are more likely to influence AuNC-membrane interactions.

In this study, internalised aggregates of AuNC were smaller than 8 nm (mean diameter of 5 nm), whereas those embedded in the peptidoglycan layer had a minimum diameter of 8.5 nm. Computational modelling has shown that small hydrophobic NPs (diameter <10 nm) can penetrate the bilayer, but become trapped in the membrane.[57] Furthermore, combined numerical and experimental studies have shown that hydrophobic NPs of diameter $d > 5$ nm (but less than 10 nm) can translocate passively through the lipid bilayer, and those NP $d \leq 5$ nm are trapped in the bilayer core and can only proceed through the bilayer when a cluster exceeding the threshold size is achieved.[34] Recent studies of the antimicrobial efficacy of AuNC of different sizes (Au_{25}, Au_{102}, and Au_{144}) demonstrate that there is a crucial internalization "size cut-off" of 2 nm (Au_{25}) that determines their antimicrobial ability; although internalisation was only proposed and not directly visualised.[20] Our previous work has shown that AuNC-ZwBuEt can freely enter the phospholipid bilayer (demonstrated by using a DOPC lipid bilayer produced in a microfluidic device). In the presence of serum, more hydrophobic particles (AuNC-ZwBuEt) could be inserted into the lipid bilayer with greater efficiency.[27]

Thus, the antibacterial action of AuNCs used in this study may be related to their binding to internal cell components such as the cytoskeletal network (actin-like protein) and ribosomes, rather than incurring damage at the membrane, since they are likely to be able to freely navigate the bacterial membrane. Indeed, cryo-SXT experiments revealed the formation of hollow intracellular vesicles (like endosomes/vacuoles observed in mammalian cells) as early as 15 min. The vesicles are not membrane bound, as would be the case for mesosomes or periplasmic vacuoles, leading to the assumption that the inclusions are caused by a stress response to internalisation of AuNC in gram-negative bacteria.

It was previously discerned by TEM analysis that pyrimidine-capped 3 nm NPs can bind to the genetic material of the cell; NPs were observed to interact with ribosomes and chromosomes and were also localised to the outer membrane peptidoglycan layer, cytoplasmic membrane and within the cytoplasm. The ability of pyrimidine-capped NPs to bind to DNA and other organelles responsible for protein synthesis was directly correlated to the extent of antibacterial activity.[8] However, DNA damage incurred from binding events between nucleic acid and NPs occur mainly with positively charged NPs, independent of NP size.[58] Indeed, highly charged NPs bind to nucleic acids and reach a stable conformation more rapidly than NPs with low charge.[59] Conversely, thiolated AuNPs have been observed to interact heavily with cytoplasmic protein and carbohydrates, rather than DNA.[23] In this work, DNA fragmentation because of AuNC-DNA interactions was not observed. Thus, since AuNC are not likely to bind directly to nucleic acids, the antimicrobial action of AuNCs may be a result of their propensity to form protein complexes within the cytoplasm,[46, 60] destroying the cytoskeletal network and forcing the condensation of chromatin.[45] Indeed, TEM imaging clearly shows the formation of fibrous AuNC-cytosolic complexes that may be attributed to break-down of the actin-like protein network within bacteria.

4. CONCLUSIONS

Herein, we investigated the antibacterial action of ultra-small AuNC (2 nm diameter) toward two common human pathogens, *S. aureus* and *P. aeruginosa,* using a combination of fluorescence and electron microscopy techniques, including cryo-SXT. AuNCs were functionalised with two surface ligands (MHA; ZwBuEt) to control cell-membrane interactions *via* a variable degree of particle hydrophobicity and/or lipophilicity and to assess the impact of such functionalisation on antibacterial activity. The variation of antibacterial efficacy of AuNC-MHA and AuNC-ZwBuEt was shown to be concentration-, time-, and strain-species-dependent. Both AuNCs displayed comparable antibacterial efficacy, irrespective of surface chemistry. However, *P. aeruginosa* showed much greater susceptibility to the bactericidal action of AuNCs. Our results obtained from a combination of complementary and independent high-resolution imaging techniques suggest that the antibacterial action was directly linked to translocation of the AuNC into the cytoplasm, as evidenced by the localisation of AuNC inside the bacterial cells. It is proposed that AuNC do not damage the membrane as they are freely translocated but cause devastating internal damage most likely by binding to the cytoskeletal network and other proteins necessary for cell function, and without compromising the nucleoid. Future work is necessary to elucidate the molecular details of interaction between AuNC and bacterial proteins. In addition, the ease of surface modification of gold NPs, *i.e.,* conjugation with antibacterial molecules, may aid in the the search for new antibacterial agents without complex chemical synthesis or sophisticated techniques. *P. aeruginosa* bacterial cells are usually resistant to a wide variety of hydrophilic antibacterial agents due to the low permeability of its outer membrane,[61] thus it is of particular interest to develop antimicrobial agents that can efficiently navigate the bacterial cell wall and membrane in order to exert maximal antimicrobial effect while minimising the generation of antimicrobial resistance.

5. EXPERIMENTAL SECTION

5.1. Synthesis of AuNCs

Chemical products were purchased in Sigma-Aldrich (France) and deionized water was used for all synthesis.

AuNCs stabilized by 6- mercaptohexanoic acid (MHA, $C_6H_{12}O_2S$, M= 148.2g mol^{-1}) was synthesized following a slightly modified protocol described elsewhere.[37] To produce AuNC-MHA with the molar ratio Au: MHA: $NaBH_4$= 1: 2: 0.4, 500 µL of $HAuCl_4.3H_20$ (20 mM) was added to 4.8 mL water followed by 4 mL of the thiolated ligand MHA (5 mM), changing the color from yellowish to pale yellow and cloudy. After 1 min, 500 µL of NaOH (1M) was added dropwise leading to almost colorless sol. After 5 min, 200 µL $NaBH_4$ (20 mM in 0.2 M NaOH) was introduced dropwise under mild stirring at 350 rpm for 4 h. Purification of the AuNC-MHA on 3 kDa cut-off filter column (Amicon) was repeated 3 times to stop the reaction, adjusted to pH7, concentrated to 2 mg Au mL^{-1} in water and kept stored in the fridge.

A modified thioctic-zwitterion (ZwBuEt, $C_{19}H_{38}N_2O_4S_3$, M=455.2 g mol^{-1}) was synthesized following the protocol described elsewhere[27]. Au NCs with zwitterion (AuZwBuEt), were prepared by the addition of gold salt ($HAuCl4.3H_2O$, 50 mM) to an alkaline solution (pH 10) containing the ligand in the presence of the reducing agent $NaBH_4$ (50mM) and stirred for 15 hours. Zwitterion stabilized AuNCs were synthesized with the molar ratio Au: ZwBuEt: $NaBH_4$ = 1:2:2. Afterwards, solution was filtered three times with Amicon 3 kDa cut-off filters at 13,600 rpm for 20 min to remove excess free ligands, adjusted to pH 7, concentrated to 2 mg Au mL^{-1} in water and kept refrigerated until use.

5.2. Spectrophotometry

UV-VIS absorption spectra of AuNC-MHA and AuNC-ZwBuEt were collected using a Shimadzu UV-1800 spectrophotometer in transmission mode.

5.3. Small angle X-ray scattering (SAXS)

SAXS was conducted on a Bruker MicroCalix SAXS operating on a Cu-Kα microfocus source (Bruker Gmbh, Germany). Data was collected on a Pilatus 100k 2D detector with q range of 0.004 to 0.56 $Å^{-1}$, where q is the scattering vector (q = 4p sin(θ)/l, 2θ is the scattering angle and l is wavelength of the scattered radiation). Calibration was carried out using silver behenate as standard. Normalisation, primary beam masking and background subtraction was carried out in RAW.[62] Analysis was carried out using SASView (version 4.1.2, http://www.sasview.org/)[63] assuming scattering length densities of 9.47 x 10^{-6} /$Å^2$ and 126 x 10^{-6} /$Å^2$ for the water and nanoparticles respectively. As small metallic nanoparticles are known to be facetted, the data was fit assuming them to be square prisms[64] which yielded good fits over the entire scattering vector range without needing to add polydispersity.

5.4. Antibacterial activity

P. aeruginosa ATCC 9721 and *S. aureus* CIP 65.8^T were obtained from American Type Culture Collection and Culture Institute Pasteur (France), respectively, and refreshed on nutrient agar (Oxoid) for 24 h at 37 °C.

To estimate the number of viable cells following treatment with AuNCs, standard plate count methods were used. *P. aeruginosa and S. aureus* stock solutions were then serially diluted in PBS until infectious dose was achieved (1000 CFU/mL *P. aeruginosa*[65] and 100,000 CFU/mL *S. aureus*).[66] AuNCs were added to suspensions of infectious dose *P. aeruginosa* and *S. aureus* (500 µL) at concentrations of 5, 10, 25, 50, 100 and 200 µg Au mL^{-1}. AuNCs/bacterial suspensions were then incubated in a rotary shaker at 37 ºC for up to 2 h at 220 RPM. Control samples consisted of bacterial suspensions in PBS with no added AuNCs, but an equal volume of MilliQ water for each given concentration. AuNCs/bacterial suspensions and controls were then spread plated on 5 separate nutrient agar (Oxoid) plates and incubated for 24 h at 37 °C to estimate the number of viable cells indicated by colony forming units (CFU).

5.5. DNA Fragmentation Assay

P. aeruginosa was suspended in PBS at an optical density (OD_{600nm}) of 0.1. 100 µg Au mL^{-1} of each AuNC was added and bacteria-AuNC suspensions were incubated at 37 °C for 1 h under shaking (120 rpm). DNA isolation was performed using the Qiagen DNeasy PowerSoil Pro Kit. 5 µL of DNA was stained with 2 µl SYBR mix green and electrophoresed for 45 min at 100 V in a 3% agarose gel to visualize the DNA. The concentration of double-stranded (ds) and single-stranded (ss) DNA was measured using a Nanodrop^{TM} spectrophotometer.

DNA fragmentation and chromatin condensation were assessed using DAPI staining of nucleic acid in *P. aeruginosa* exposed to 100 µg Au mL^{-1} of each AuNC. Suspensions of bacteria and AuNC were prepared as described above and stained with 10 µg/ml DAPI for 20 min at room temperature. DAPI stained bacterial cells were visualised after 1 h using a Zeiss Airyscan 880 LSM instrument with a 63× objective.

5.6. Statistical analysis

All plate count experiments were performed in replicates of 5 and repeated a minimum of 2 times. Data are expressed as a mean ± standard deviation of at least 5 independent samples. Statistical comparisons were made between results using a two-tailed student's T-test where $p < 0.05$ denoted a statistically significant difference.

5.7. Transmission Electron Microscopy (TEM)

TEM was used to view cross sections of bacterial cells incubated with AuNCs. AuNCs were incubated with bacteria at concentrations of 100 µg/ml in a rotary shaker at 37 °C at 220 RPM for 30, 60 and, 120 min. Following the incubation period, the cells were washed and then fixed for TEM. After incubation, bacterial cell suspensions were washed twice with 10 mM PBS (pH of 7.4) using centrifugation at 13000 rpm for 5 min at 25°C to remove any AuNC that had not interacted with the cells. The pellets were then suspended in 2 mL of 1% glutaraldehyde in PBS for 30 min, and then washed twice in PBS for 5 min. After the final washing step, the cell suspensions were post-fixed with 1 mL of 1% aqueous osmium tetroxide (OsO_4) for 1.5 h. The cell pellets were washed 3× in nanopure H_2O (with a resistivity of 18.2 MW cm^{-1}) for 5 min each. Samples were then dehydrated by passing them through a graded ethanol series (20, 40, and 60%) (2 mL) for 20 min each and then stained for 8 h with 2% uranyl acetate in 70% ethanol (2 mL). After staining, the cells were further dehydrated by passing the samples through another graded ethanol series (80, 90 and 100%) for 15 min each (2 mL) at -20 °C.

The embedding medium was prepared using Spurr's resin (ProSciTech). To embed the samples, each sample was incubated at -20°C in 2 mL of 100% ethanol and Spurr's epoxy monomer (1:1 ratio) for 8 h, followed by a transfer to 100% ethanol and epoxy monomer (1:3 ratio) for 8 h, then finally a transfer into the pure epoxy for 8 h. Each sample was then transferred into a gelatin capsule containing fresh epoxy monomer mixed with 1% dry benzoyl peroxide, which was then polymerized for 24 h at 4°C. The final block was trimmed, then cut into ultrathin sections (50 nm thickness) using a Leica EM UC7 Ultramicrotome (Leica Microsystems, Wetzlar, Germany) with a diamond knife (Diatome, Pennsylvania, USA). Sections were placed onto 300 mesh copper grids and examined using a JEM 1010 instrument (JEOL). Approximately 40 TEM images were taken for each sample analysed.

STEM-EDS analysis was performed on samples prepared as described above using a TEM Jeol 2100F (FEG, 200 kV) equipped with a high-angle annular dark field detector (HAADF, scanning TEM mode, STEM) and energy dispersive X-ray spectrometer (EDS).

5.8. Cryo-soft-X-ray tomography

Quantifoil R 2/2 holey carbon-film microscopy grids (Au-G200F1) were exposed to 1 min O_2 plasma to increase their hydrophilicity. *P. aeruginosa* colonies from a nutrient agar plate (kept at 37°C for 24 h) were suspended in PBS at an optical density of OD_{600nm} 0.1. 100 µg Au mL^{-1} were added and AuNCs and bacteria were left to interact for ~15 min or 1 h before vitrification. Immediately prior to plunge-freezing (Leica, EM, GP), the grids were blotted from the rear using Whatman filter paper no.4 to remove excess medium, and 2 µL of Au fiducial markers with a 100 nm diameter were added to the grids for projection alignment. The distribution of the cells on the frozen grid and the ice thickness were confirmed using cryostage (CMS196 Linkam Scientific Instruments, Epsom, UK)-equipped fluorescence microscope (Zeiss Axio Scope). Grids were transferred to holders and stored in liquid nitrogen. The frozen grids were transferred to Mistral (ALBA-Light Source) beamline in ALBA synchrotron under cryogenic conditions.[67] Tomograms were collected from a tilt range of ± 65° with a step size of 1° at 2.43 nm wavelength (photon energy E = 520 eV) with a 40 nm zone and a 25 nm plate and an image pixel size of 8 nm for bacteria. Approximately ~131 images were acquired for each tilt series with exposure times varying from 1s-2s. Tilt series were aligned and reconstructed using the batch reconstruction processes in IMOD and segmentation was done with Microscopy Image Browser ver 2.70.

ASSOCIATED CONTENT

Supporting Information.

The following files are available free of charge. Characterization of AuNC. Metabolic activity of bacteria exposed to AuNC for 2 h. Dynamic antibacterial activity. TEM of bacterial morphology post AuNC exposure. SEM micrograph of bacterial morphology. Confocal laser microscopy (CLSM) analysis of Syto9 fluorescence. CLSM analysis of AuNC-ZwBuEt and AuNC-MHA uptake in *P. aeruginosa.* Reconstructed Cryo-SXT tomogram of control *P. aeruginosa* bacteria. STEM-EDS analyses of *S. aureus* and *P. aeruginosa* incubated with 100 µg ml^{-1} AuNC-MHA and AuNC-ZwBuEt. DNA fragmentation assay *via* gel electrophoresis. DAPI staining of *P. aeruginosa* DNA following incubation with AuNC. Cell surface characterisation of *P. aeruginosa* and *S. aureus.* (PDF)

AUTHOR INFORMATION

***Corresponding author:** elena.ivanova@rmit.edu.au **– Phone number : +61 3 99 253 395**

Author Contributions

The manuscript was written through contributions of all authors. All authors have given approval to the final version of the manuscript.

Funding from the Australian Research Council (ARC) Industrial Transformation Research Hubs scheme (project number IH130100017) and the ARC Industrial Transformation Training Centre scheme (project number IC180100005) to E.P.I. is thankfully acknowledged. XLG would like to thank ANR SIREN (ANR-20-CE92-0039-01) and ANR LAPIN (ANR-20-CE09-0021-04) for their financial support.

NOTES

The authors declare that there is no conflict of interest

ACKNOWLEDGMENTS

The authors acknowledge the support and technical services of the RMIT Microscopy and Microanalysis Facility (RMMF). D.P.L acknowledges receipt of the internship AINSE ANSTO French Embassy (SAAFE) for travel support. The authors acknowledge travel funding provided by the International Synchrotron Access Program (ISAP) managed by the Australian Synchrotron, part of ANSTO. This work was performed in part at the Mistral beamline at ALBA synchrotron, Spain. XLG would like to thank Agence National de la Recherche (ANR PRC LAPIN; ANR PRCI SIREN). We thank J. Groen (ALBA) for his support in sample preparation.

REFERENCES

(1) Nair, L. V.; Nair, R. V.; Shenoy, S. J.; Thekkuveettil, A.; Jayasree, R. S. Blood Brain Barrier Permeable Gold Nanocluster for Targeted Brain Imaging and Therapy: An in Vitro and in Vivo Study. *J. Mater. Chem. B.* **2017,** *5* (42), 8314-8321, DOI: 10.1039/c7tb02247f.

(2) Yu, Z.; Musnier, B.; Wegner, K. D.; Henry, M.; Chovelon, B.; Desroches-Castan, A.; Fertin, A.; Resch-Genger, U.; Bailly, S.; Coll, J.-L.; Usson, Y.; Josserand, V.; Le Guével, X. High-Resolution Shortwave Infrared Imaging of Vascular Disorders Using Gold Nanoclusters. *ACS Nano* **2020,** *14* (4), 4973-4981, DOI: 10.1021/acsnano.0c01174.

(3) Tang, S.; Peng, C.; Xu, J.; Du, B.; Wang, Q.; Vinluan, R. D., 3rd; Yu, M.; Kim, M. J.; Zheng, J. Tailoring Renal Clearance and Tumor Targeting of Ultrasmall Metal Nanoparticles with Particle Density. *Angew. Chem. Int. Ed.* **2016,** *55* (52), 16039-16043, DOI: 10.1002/anie.201609043.

(4) Loynachan, C. N.; Soleimany, A. P.; Dudani, J. S.; Lin, Y.; Najer, A.; Bekdemir, A.; Chen, Q.; Bhatia, S. N.; Stevens, M. M. Renal Clearable Catalytic Gold Nanoclusters for

in Vivo Disease Monitoring. *Nat Nanotechnol* **2019,** *14* (9), 883-890, DOI: 10.1038/s41565-019-0527-6.

(5) Colombé, C.; Le Guével, X.; Martin-Serrano, A.; Henry, M.; Porret, E.; Comby-Zerbino, C.; Antoine, R.; Atallah, I.; Busser, B.; Coll, J.-L.; Righini, C. A.; Sancey, L. Gold Nanoclusters as a Contrast Agent for Image-Guided Surgery of Head and Neck Tumors. *Nanomed.: Nanotechnol. Biol. Med.* **2019,** *20*, 102011, DOI: 10.1016/j.nano.2019.04.014.

(6) Le Guével, X.; Henry, M.; Motto-Ros, V.; Longo, E.; Montañez, M. I.; Pelascini, F.; de La Rochefoucauld, O.; Zeitoun, P.; Coll, J.-L.; Josserand, V.; Sancey, L. Elemental and Optical Imaging Evaluation of Zwitterionic Gold Nanoclusters in Glioblastoma Mouse Models. *Nanoscale* **2018,** *10* (39), 18657-18664, DOI: 10.1039/c8nr05299a.

(7) Chen, Y.; Montana, D. M.; Wei, H.; Cordero, J. M.; Schneider, M.; Le Guével, X.; Chen, O.; Bruns, O. T.; Bawendi, M. G. Shortwave Infrared in Vivo Imaging with Gold Nanoclusters. *Nano Lett.* **2017,** *17* (10), 6330-6334, DOI: 10.1021/acs.nanolett.7b03070.

(8) Zhao, Y.; Tian, Y.; Cui, Y.; Liu, W.; Ma, W.; Jiang, X. Small Molecule-Capped Gold Nanoparticles as Potent Antibacterial Agents That Target Gram-Negative Bacteria. *J. Am. Chem. Soc.* **2010,** *132* (35), 12349-12356, DOI: 10.1021/ja1028843.

(9) Shamaila, S.; Zafar, N.; Riaz, S.; Sharif, R.; Nazir, J.; Naseem, S. Gold Nanoparticles: An Efficient Antimicrobial Agent against Enteric Bacterial Human Pathogen. *Nanomaterials (Basel)* **2016,** *6* (4), 71, DOI: 10.3390/nano6040071.

(10) Zheng, K.; Setyawati, M. I.; Leong, D. T.; Xie, J. Antimicrobial Gold Nanoclusters. *ACS Nano* **2017,** *11* (7), 6904-6910, DOI: 10.1021/acsnano.7b02035.

(11) Yougbare, S.; Chang, T.-K.; Tan, S.-H.; Kuo, J.-C.; Hsu, P.-H.; Su, C.-Y.; Kuo, T.-R. Antimicrobial Gold Nanoclusters: Recent Developments and Future Perspectives. *Int. J. Mol. Sci.* **2019,** *20* (12), 2924, DOI: 10.3390/ijms20122924.

(12) Tran, P. A.; O'Brien-Simpson, N.; Palmer, J. A.; Bock, N.; Reynolds, E. C.; Webster, T. J.; Deva, A.; Morrison, W. A.; O'Connor, A. J. Selenium Nanoparticles as Anti-Infective Implant Coatings for Trauma Orthopedics against Methicillin-Resistant *Staphylococcus Aureus* and Epidermidis: In Vitro and in Vivo Assessment. *Int. J. Nanomedicine* **2019,** *14*, 4613-4624, DOI: 10.2147/IJN.S197737.

(13) Kalita, S.; Kandimalla, R.; Bhowal, A. C.; Kotoky, J.; Kundu, S. Functionalization of B-Lactam Antibiotic on Lysozyme Capped Gold Nanoclusters Retrogress Mrsa and Its Persisters Following Awakening. *Sci. Rep.* **2018,** *8* (1), 5778-5778, DOI: 10.1038/s41598-018-22736-5.

(14) Zheng, Y.; Liu, W.; Qin, Z.; Chen, Y.; Jiang, H.; Wang, X. Mercaptopyrimidine-Conjugated Gold Nanoclusters as Nanoantibiotics for Combating Multidrug-Resistant Superbugs. *Bioconjugate Chem.* **2018,** *29* (9), 3094-3103, DOI: 10.1021/acs.bioconjchem.8b00452.

(15) Xie, Y.; Zhang, M.; Zhang, W.; Liu, X.; Zheng, W.; Jiang, X. Gold Nanoclusters-Coated Orthodontic Devices Can Inhibit the Formation of *Streptococcus* Mutans Biofilm. *ACS Biomater. Sci. Eng.* **2020,** *6* (2), 1239-1246, DOI: 10.1021/acsbiomaterials.9b01647.

(16) Pang, Z.; Li, Q.; Jia, Y.; Yan, W.; Qi, J.; Guo, Y.; Hu, F.; Zhou, D.; Jiang, X. Controlling the Pyridinium-Zwitterionic Ligand Ratio on Atomically Precise Gold Nanoclusters Allowing for Eradicating Gram-Positive Drug-Resistant Bacteria and

Retaining Biocompatibility. *Chem Sci* **2021,** *12* (44), 14871-14882, DOI: 10.1039/d1sc03056f.

(17) Zheng, K.; Setyawati, M. I.; Leong, D. T.; Xie, J. Surface Ligand Chemistry of Gold Nanoclusters Determines Their Antimicrobial Ability. *Chem. Mater.* **2018,** *30* (8), 2800-2808, DOI: 10.1021/acs.chemmater.8b00667.

(18) Lin, Y.; Ren, J.; Qu, X. Catalytically Active Nanomaterials: A Promising Candidate for Artificial Enzymes. *Acc. Chem. Res.* **2014,** *47* (4), 1097-1105, DOI: 10.1021/ar400250z.

(19) Xie, Y.; Liu, Y.; Yang, J.; Liu, Y.; Hu, F.; Zhu, K.; Jiang, X. Gold Nanoclusters for Targeting Methicillin-Resistant *Staphylococcus Aureus* in Vivo. *Angew. Chem. Int. Ed.* **2018,** *57* (15), 3958-3962, DOI: 10.1002/anie.201712878.

(20) Zheng, K.; Setyawati, M. I.; Leong, D. T.; Xie, J. Overcoming Bacterial Physical Defenses with Molecule-Like Ultrasmall Antimicrobial Gold Nanoclusters. *Bioact Mater* **2020,** *6* (4), 941-950, DOI: 10.1016/j.bioactmat.2020.09.026.

(21) Kuo, J.-C.; Tan, S.-H.; Hsiao, Y.-C.; Mutalik, C.; Chen, H.-M.; Yougbaré, S.; Kuo, T.-R. Unveiling the Antibacterial Mechanism of Gold Nanoclusters Via in Situ Transmission Electron Microscopy. *ACS Sustainable Chemistry & Engineering* **2022,** *10* (1), 464-471, DOI: 10.1021/acssuschemeng.1c06714.

(22) Ortiz-Benitez, E. A.; Carrillo-Morales, M.; Velázquez-Guadarrama, N.; Fandiño-Armas, J.; Olivares-Trejo, J. d. J. Inclusion Bodies and Ph Lowering: As an Effect of Gold Nanoparticles in Streptococcus Pneumoniae. *Metallomics* **2015,** *7* (7), 1173-1179, DOI: 10.1039/c5mt00044k.

(23) Ortiz-Benítez, E. A.; Velázquez-Guadarrama, N.; Durán Figueroa, N. V.; Quezada, H.; Olivares-Trejo, J. d. J. Antibacterial Mechanism of Gold Nanoparticles Onstreptococcus Pneumoniae. *Metallomics* **2019,** *11* (7), 1265-1276, DOI: 10.1039/c9mt00084d.

(24) Zhang, H.; Liu, H.; Tian, Z.; Lu, D.; Yu, Y.; Cestellos-Blanco, S.; Sakimoto, K. K.; Yang, P. Bacteria Photosensitized by Intracellular Gold Nanoclusters for Solar Fuel Production. *Nat Nanotechnol* **2018,** *13* (10), 900-905, DOI: 10.1038/s41565-018-0267-z.

(25) Reniere, M. L. Reduce, Induce, Thrive: Bacterial Redox Sensing During Pathogenesis. *J Bacteriol* **2018,** *200* (17), e00128-18, DOI: 10.1128/JB.00128-18.

(26) Chithrani, B. D.; Ghazani, A. A.; Chan, W. C. W. Determining the Size and Shape Dependence of Gold Nanoparticle Uptake into Mammalian Cells. *Nano Lett.* **2006,** *6* (4), 662-668, DOI: 10.1021/nl052396o.

(27) Porret, E.; Sancey, L.; Martín-Serrano, A.; Montañez, M. I.; Seeman, R.; Yahia-Ammar, A.; Okuno, H.; Gomez, F.; Ariza, A.; Hildebrandt, N.; Fleury, J.-B.; Coll, J.-L.; Le Guével, X. Hydrophobicity of Gold Nanoclusters Influences Their Interactions with Biological Barriers. *Chem. Mater.* **2017,** *29* (17), 7497-7506, DOI: 10.1021/acs.chemmater.7b02497.

(28) Tay, C. Y.; Yu, Y.; Setyawati, M. I.; Xie, J.; Leong, D. T. Presentation Matters: Identity of Gold Nanocluster Capping Agent Governs Intracellular Uptake and Cell Metabolism. *Nano Res.* **2014,** *7* (6), 805-815, DOI: 10.1007/s12274-014-0441-z.

(29) Carnovale, C.; Bryant, G.; Shukla, R.; Bansal, V. Identifying Trends in Gold Nanoparticle Toxicity and Uptake: Size, Shape, Capping Ligand, and Biological Corona. *ACS Omega* **2019,** *4* (1), 242-256, DOI: 10.1021/acsomega.8b03227.

(30) Porret, E.; Le Guével, X.; Coll, J.-L. Gold Nanoclusters for Biomedical Applications: Toward in Vivo Studies. *J. Mater. Chem. B.* **2020,** *8* (11), 2216-2232, DOI: 10.1039/c9tb02767j.

(31) Genji Srinivasulu, Y.; Yao, Q.; Goswami, N.; Xie, J. Interfacial Engineering of Gold Nanoclusters for Biomedical Applications. *Mater. Horiz.* **2020,** *7* (10), 2596-2618, DOI: 10.1039/d0mh00827c.

(32) Yang, K.; Ma, Y.-Q. Computer Simulation of the Translocation of Nanoparticles with Different Shapes across a Lipid Bilayer. *Nat Nanotechnol* **2010,** *5* (8), 579-583, DOI: 10.1038/nnano.2010.141.

(33) Pogodin, S.; A. Baulin, V. Equilibrium Insertion of Nanoscale Objects into Phospholipid Bilayers. *Curr. Nanosci.* **2011,** *7* (5), 721-726, DOI: 10.2174/157341311797483871.

(34) Guo, Y.; Terazzi, E.; Seemann, R.; Fleury, J. B.; Baulin, V. A. Direct Proof of Spontaneous Translocation of Lipid-Covered Hydrophobic Nanoparticles through a Phospholipid Bilayer. *Sci Adv* **2016,** *2* (11), e1600261-e1600261, DOI: 10.1126/sciadv.1600261.

(35) Yuan, X.; Goswami, N.; Chen, W.; Yao, Q.; Xie, J. Insights into the Effect of Surface Ligands on the Optical Properties of Thiolated Au25nanoclusters. *ChemComm* **2016,** *52* (30), 5234-5237, DOI: 10.1039/c6cc00857g.

(36) Ivanov, M. R.; Haes, A. J. Anionic Functionalized Gold Nanoparticle Continuous Full Filling Separations: Importance of Sample Concentration. *Anal. Chem.* **2012,** *84* (3), 1320-1326, DOI: 10.1021/ac2022376.

(37) Musnier, B.; Wegner, K. D.; Comby-Zerbino, C.; Trouillet, V.; Jourdan, M.; Häusler, I.; Antoine, R.; Coll, J.-L.; Resch-Genger, U.; Le Guével, X. High Photoluminescence of Shortwave Infrared-Emitting Anisotropic Surface Charged Gold Nanoclusters. *Nanoscale* **2019,** *11* (25), 12092-12096, DOI: 10.1039/c9nr04120f.

(38) Zhao, S.; Austin, N.; Li, M.; Song, Y.; House, S. D.; Bernhard, S.; Yang, J. C.; Mpourmpakis, G.; Jin, R. Influence of Atomic-Level Morphology on Catalysis: The Case of Sphere and Rod-Like Gold Nanoclusters for Co2 Electroreduction. *ACS Catal.* **2018,** *8* (6), 4996-5001, DOI: 10.1021/acscatal.8b00365.

(39) Li, Q.; Zeman, C. J.; Ma, Z.; Schatz, G. C.; Gu, X. W. Bright Nir-Ii Photoluminescence in Rod-Shaped Icosahedral Gold Nanoclusters. *Small* **2021,** *17* (11), 2007992, DOI: 10.1002/smll.202007992.

(40) Zhou, M.; Jin, R.; Sfeir, M. Y.; Chen, Y.; Song, Y.; Jin, R. Electron Localization in Rod-Shaped Triicosahedral Gold Nanocluster. *Proc. Natl. Acad. Sci. U.S.A.* **2017,** *114* (24), E4697-E4705, DOI: 10.1073/pnas.1704699114.

(41) Fernández, T. D.; Pearson, J. R.; Leal, M. P.; Torres, M. J.; Blanca, M.; Mayorga, C.; Le Guével, X. Intracellular Accumulation and Immunological Properties of Fluorescent Gold Nanoclusters in Human Dendritic Cells. *Biomaterials* **2015,** *43*, 1-12, DOI: 10.1016/j.biomaterials.2014.11.045.

(42) Otón, J.; Pereiro, E.; Pérez-Berná, A. J.; Millach, L.; Sorzano, C. O. S.; Marabini, R.; Carazo, J. M. Characterization of Transfer Function, Resolution and Depth of Field of a Soft X-Ray Microscope Applied to Tomography Enhancement by Wiener Deconvolution. *Biomed Opt Express* **2016,** *7* (12), 5092-5103, DOI: 10.1364/BOE.7.005092.

(43) Rezaei, A.; Hashemi, E. A Pseudohomogeneous Nanocarrier Based on Carbon Quantum Dots Decorated with Arginine as an Efficient Gene Delivery Vehicle. *Sci. Rep.* **2021,** *11* (1), 13790-13790, DOI: 10.1038/s41598-021-93153-4.

(44) Vukomanovic, M.; Cendra, M. d. M.; Baelo, A.; Torrents, E. Nano-Engineering Stable Contact-Based Antimicrobials: Chemistry at the Interface between Nano-Gold and Bacteria. *Colloids Surf. B: Biointerfaces* **2021,** *208*, 112083, DOI: 10.1016/j.colsurfb.2021.112083.

(45) Feng, Q. L.; Wu, J.; Chen, G. Q.; Cui, F. Z.; Kim, T. N.; Kim, J. O. A Mechanistic Study of the Antibacterial Effect of Silver Ions on *Escherichia Coli* and *Staphylococcus Aureus*. *J. Biomed. Mater. Res.* **2000,** *52* (4), 662-668, DOI: 10.1002/1097-4636(20001215)52:4<662::aid-jbm10>3.0.co;2-3.

(46) Slavin, Y. N.; Asnis, J.; Häfeli, U. O.; Bach, H. Metal Nanoparticles: Understanding the Mechanisms Behind Antibacterial Activity. *J. Nanobiotechnology* **2017,** *15* (1), 65-65, DOI: 10.1186/s12951-017-0308-z.

(47) Pajerski, W.; Ochonska, D.; Brzychczy-Wloch, M.; Indyka, P.; Jarosz, M.; Golda-Cepa, M.; Sojka, Z.; Kotarba, A. Attachment Efficiency of Gold Nanoparticles by Gram-Positive and Gram-Negative Bacterial Strains Governed by Surface Charges. *J. Nanoparticle Res.* **2019,** *21* (8), 186, DOI: 10.1007/s11051-019-4617-z.

(48) Hwang, G. B.; Huang, H.; Wu, G.; Shin, J.; Kafizas, A.; Karu, K.; Toit, H. D.; Alotaibi, A. M.; Mohammad-Hadi, L.; Allan, E.; MacRobert, A. J.; Gavriilidis, A.; Parkin, I. P. Photobactericidal Activity Activated by Thiolated Gold Nanoclusters at Low Flux Levels of White Light. *Nat Commun* **2020,** *11* (1), 1207-1207, DOI: 10.1038/s41467-020-15004-6.

(49) Preston, T. C.; Nuruzzaman, M.; Jones, N. D.; Mittler, S. Role of Hydrogen Bonding in the Ph-Dependent Aggregation of Colloidal Gold Particles Bearing Solution-Facing Carboxylic Acid Groups. *J. Phys. Chem. C* **2009,** *113* (32), 14236-14244, DOI: 10.1021/jp903284h.

(50) Goodman, C. M.; McCusker, C. D.; Yilmaz, T.; Rotello, V. M. Toxicity of Gold Nanoparticles Functionalized with Cationic and Anionic Side Chains. *Bioconjugate Chem.* **2004,** *15* (4), 897-900, DOI: 10.1021/bc049951i.

(51) Pfeiffer, T.; De Nicola, A.; Montis, C.; Carlà, F.; van der Vegt, N. F. A.; Berti, D.; Milano, G. Nanoparticles at Biomimetic Interfaces: Combined Experimental and Simulation Study on Charged Gold Nanoparticles/Lipid Bilayer Interfaces. *J. Phys. Chem. Lett.* **2018,** *10* (2), 129-137, DOI: 10.1021/acs.jpclett.8b03399.

(52) Wei, X.; Yu, J.; Ding, L.; Hu, J.; Jiang, W. Effect of Oxide Nanoparticles on the Morphology and Fluidity of Phospholipid Membranes and the Role of Hydrogen Bonds. *J. Environ. Sci.* **2017,** *57*, 221-230, DOI: 10.1016/j.jes.2017.02.011.

(53) Zhang, S.; Nelson, A.; Beales, P. A. Freezing or Wrapping: The Role of Particle Size in the Mechanism of Nanoparticle–Biomembrane Interaction. *Langmuir* **2012,** *28* (35), 12831-12837, DOI: 10.1021/la301771b.

(54) Verma, A.; Uzun, O.; Hu, Y.; Hu, Y.; Han, H.-S.; Watson, N.; Chen, S.; Irvine, D. J.; Stellacci, F. Surface-Structure-Regulated Cell-Membrane Penetration by Monolayer-Protected Nanoparticles. *Nat. Mater.* **2008,** *7* (7), 588-595, DOI: 10.1038/nmat2202.

(55) Van Lehn, R. C.; Atukorale, P. U.; Carney, R. P.; Yang, Y.-S.; Stellacci, F.; Irvine, D. J.; Alexander-Katz, A. Effect of Particle Diameter and Surface Composition on the

Spontaneous Fusion of Monolayer-Protected Gold Nanoparticles with Lipid Bilayers. *Nano Lett.* **2013,** *13* (9), 4060-4067, DOI: 10.1021/nl401365n.

(56) Canepa, E.; Salassi, S.; Simonelli, F.; Ferrando, R.; Rolandi, R.; Lambruschini, C.; Canepa, F.; Dante, S.; Relini, A.; Rossi, G. Non-Disruptive Uptake of Anionic and Cationic Gold Nanoparticles in Neutral Zwitterionic Membranes. *Sci. Rep.* **2021,** *11* (1), 1256, DOI: 10.1038/s41598-020-80953-3.

(57) Li, Y.; Chen, X.; Gu, N. Computational Investigation of Interaction between Nanoparticles and Membranes: Hydrophobic/Hydrophilic Effect. *J. Phys. Chem. B* . **2008,** *112* (51), 16647-16653, DOI: 10.1021/jp8051906.

(58) May, S.; Hirsch, C.; Rippl, A.; Bohmer, N.; Kaiser, J.-P.; Diener, L.; Wichser, A.; Bürkle, A.; Wick, P. Transient DNA Damage Following Exposure to Gold Nanoparticles. *Nanoscale* **2018,** *10* (33), 15723-15735, DOI: 10.1039/c8nr03612h.

(59) Nash, J. A.; Tucker, T. L.; Therriault, W.; Yingling, Y. G. Binding of Single Stranded Nucleic Acids to Cationic Ligand Functionalized Gold Nanoparticles. *Biointerphases* **2016,** *11* (4), 04B305, DOI: 10.1116/1.4966653.

(60) Wigginton, N. S.; Titta, A. d.; Piccapietra, F.; Dobias, J.; Nesatyy, V. J.; Suter, M. J. F.; Bernier-Latmani, R. Binding of Silver Nanoparticles to Bacterial Proteins Depends on Surface Modifications and Inhibits Enzymatic Activity. *Environ. Sci. Technol.* **2010,** *44* (6), 2163-2168, DOI: 10.1021/es903187s.

(61) Yoshimura, F.; Nikaido, H. Permeability of *Pseudomonas Aeruginosa* Outer Membrane to Hydrophilic Solutes. *J Bacteriol* **1982,** *152* (2), 636-642, DOI: 10.1128/jb.152.2.636-642.1982.

(62) Hopkins, J. B.; Gillilan, R. E.; Skou, S. Bioxtas Raw: Improvements to a Free Open-Source Program for Small-Angle X-Ray Scattering Data Reduction and Analysis. *J. Appl. Crystallogr.* **2017,** *50* (Pt 5), 1545-1553, DOI: 10.1107/S1600576717011438.

(63) Bakker, J. H.; Washington, A. L.; Parnell, S. R.; van Well, A. A.; Pappas, C.; Bouwman, W. G. Analysis of Sesans Data By numerical hankel Transform Implementation in sasview. *J. Neutron Res.* **2020,** *22* (1), 57-70, DOI: 10.3233/jnr-200154.

(64) Nayuk, R.; Huber, K. Formfactors of Hollow and Massive Rectangular Parallelepipeds at Variable Degree of Anisometry. *Z. Phys. Chem.* **2012,** *226* (7-8), 837-854, DOI: 10.1524/zpch.2012.0257.

(65) Leggett, H. C.; Cornwallis, C. K.; West, S. A. Mechanisms of Pathogenesis, Infective Dose and Virulence in Human Parasites. *PLoS Pathog.* **2012,** *8* (2), e1002512-e1002512, DOI: 10.1371/journal.ppat.1002512.

(66) Passon, T. Methicillin-Resistant Staphylococcus Aureus: A Public Health Response to New Threats of Staph Infection. *The Synergist* **2007,** *18* (11), 35, DOI: 10.3320/1.2904739.

(67) Sorrentino, A.; Nicolás, J.; Valcárcel, R.; Chichón, F. J.; Rosanes, M.; Avila, J.; Tkachuk, A.; Irwin, J.; Ferrer, S.; Pereiro, E. Mistral: A Transmission Soft X-Ray Microscopy Beamline for Cryo Nano-Tomography of Biological Samples and Magnetic Domains Imaging. *J. Synchrotron Radiat.* **2015,** *22* (4), 1112-1117, DOI: 10.1107/s1600577515008632.

TOC Graphic

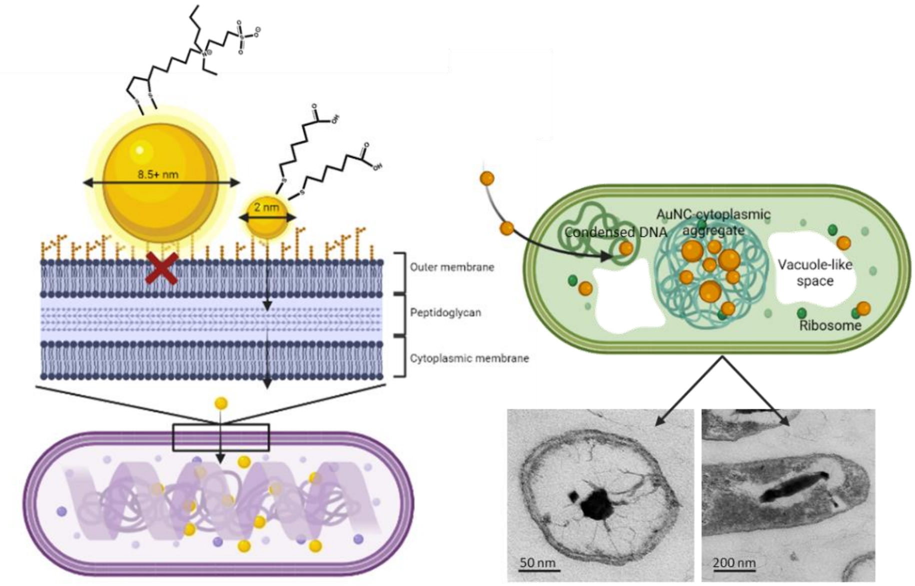
8.5+ nm
2 nm
Outer membrane
Peptidoglycan
Cytoplasmic membrane
Condensed DNA
AuNC cytoplasmic aggregate
Vacuole-like space
Ribosome
50 nm
200 nm